










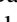







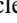
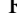











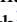




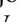


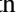

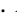





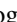


















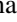

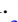





















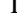














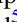







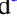




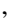













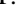

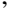





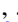

















Publication Year	2021
Acceptance in OA @INAF	2022-06-07T14:08:47Z
Title	Space Telescope and Optical Reverberation Mapping Project. IX. Velocity-Delay Maps for Broad Emission Lines in NGC 5548
Authors	Horne, Keith; Rosa, G. De; Peterson, B. M.; Barth, A. J.; Ely, J.; et al.
DOI	10.3847/1538-4357/abce60
Handle	http://hdl.handle.net/20.500.12386/32222
Journal	THE ASTROPHYSICAL JOURNAL
Number	907



Space Telescope and Optical Reverberation Mapping Project. IX. Velocity–Delay Maps for Broad Emission Lines in NGC 5548

Keith Horne¹ , G. De Rosa² , B. M. Peterson^{2,3,4} , A. J. Barth⁵ , J. Ely² , M. M. Fausnaugh^{3,6} , G. A. Kriss² , L. Pei⁵ , M. C. Bentz⁷ , E. M. Cackett⁸ , R. Edelson⁹ , M. Eracleous^{10,11} , M. R. Goad¹² , C. J. Grier^{3,13} , J. Kaastra^{14,15} , C. S. Kochanek^{3,4} , Y. Krongold¹⁶ , S. Mathur^{3,4} , H. Netzer¹⁷ , D. Proga¹⁸ , N. Tejos¹⁹ , M. Vestergaard^{13,20} , C. Villforth²¹ , S. M. Adams^{3,22} , M. D. Anderson⁷ , P. Arévalo²³ , T. G. Beatty^{3,24} , V. N. Bennert²⁵ , A. Bigley²⁶ , S. Bisogni^{3,27} , G. A. Borman²⁸ , T. A. Boroson²⁹ , M. C. Bottorff³⁰ , W. N. Brandt^{10,11,31} , A. A. Breeveld³² , M. Brotherton³³ , J. E. Brown³⁴ , J. S. Brown^{3,35} , G. Canalizo³⁶ , M. T. Carini³⁷ , K. I. Clubb²⁶ , J. M. Comerford³⁸ , E. M. Corsini^{39,40} , D. M. Crenshaw⁷ , S. Croft²⁶ , K. V. Croxall^{3,4} , E. Dalla Bontà^{39,40} , A. J. Deason^{41,42} , M. Dehghanian⁴³ , A. De Lorenzo-Cáceres^{1,44} , K. D. Denney^{3,4} , M. Dietrich^{45,100} , C. Done⁴⁶ , N. V. Efimova⁴⁷ , P. A. Evans¹² , G. J. Ferland⁴³ , A. V. Filippenko^{26,48} , K. Flatland^{49,50} , O. D. Fox^{2,26} , E. Gardner^{46,51} , E. L. Gates⁵² , N. Gehrels^{53,101} , S. Geier^{54,55,56} , J. M. Gelbord^{57,58} , L. Gonzalez⁴⁹ , V. Gorjian⁵⁹ , J. E. Greene⁶⁰ , D. Grupe⁶¹ , A. Gupta³ , P. B. Hall⁶² , C. B. Henderson^{3,63} , S. Hicks³⁷ , E. Holmbeck⁶⁴ , T. W.-S. Holoien^{3,4,65} , T. Hutchison^{30,66,67} , M. Im⁶⁸ , J. J. Jensen²⁰ , C. A. Johnson⁶⁹ , M. D. Joner⁷⁰ , J. Jones⁷ , S. Kaspi^{17,71} , P. L. Kelly^{26,72} , J. A. Kennea¹⁰ , M. Kim^{73,74} , S. Kim^{3,4,75} , S. C. Kim⁷³ , A. King⁷⁶ , S. A. Klimanov⁴⁷ , K. T. Korista⁷⁷ , M. W. Lau³⁶ , J. C. Lee⁷³ , D. C. Leonard⁴⁹ , Miao Li⁷⁸ , P. Lira⁷⁹ , C. Lochhaas^{2,3} , Zhiyuan Ma⁸⁰ , F. MacInnis³⁰ , M. A. Malkan⁶⁴ , E. R. Manne-Nicholas⁷ , J. C. Mauerhan²⁶ , R. McGurk^{41,65} , I. M. McHardy⁸¹ , C. Montuori⁸² , L. Morelli^{39,40,83} , A. Mosquera^{3,84} , D. Mudd³ , F. Müller-Sánchez^{38,85} , S. V. Nazarov²⁸ , R. P. Norris⁷ , J. A. Nousek¹⁰ , M. L. Nguyen³³ , P. Ochner^{39,40} , D. N. Okhat²⁸ , A. Pancoast⁸⁶ , I. Papadakis^{87,88} , J. R. Parks⁷ , M. T. Penny^{3,89} , A. Pizzella^{39,40} , R. W. Pogge^{3,4} , R. Poleski³ , J.-U. Pott⁹⁰ , S. E. Rafter^{71,91} , H.-W. Rix⁹⁰ , J. Runnoe^{92,93} , D. A. Saylor⁷ , J. S. Schimoia^{3,94} , K. Schnülle⁹⁰ , B. Scott³⁶ , S. G. Sergeev²⁸ , B. J. Shappee^{3,95} , I. Shivvers²⁶ , M. Siegel²⁹ , G. V. Simonian³ , A. Siviero³⁹ , A. Skielboe²⁰ , G. Somers^{3,93} , M. Spencer⁷⁰ , D. Starkey^{1,96} , D. J. Stevens^{3,10,24} , H.-I. Sung⁷³ , J. Tayar^{3,95,102} , T. Treu^{64,103} , C. S. Turner⁷ , P. Uttley⁹⁷ , J. Van Saders^{3,95} , L. Vican⁶⁴ , S. Villanueva, Jr.^{3,98,105} , Y. Weiss⁷¹ , J.-H. Woo⁶⁸ , H. Yan³⁴ , S. Young⁹ , H. Yuk²⁶ , W. Zheng²⁶ , W. Zhu³ , and Y. Zu^{3,99} 

¹ SUPA Physics and Astronomy, University of St. Andrews, Fife, KY16 9SS, UK

² Space Telescope Science Institute, 3700 San Martin Drive, Baltimore, MD 21218, USA

³ Department of Astronomy, The Ohio State University, 140 W 18th Ave., Columbus, OH 43210, USA

⁴ Center for Cosmology and AstroParticle Physics, The Ohio State University, 191 West Woodruff Ave., Columbus, OH 43210, USA

⁵ Department of Physics and Astronomy, 4129 Frederick Reines Hall, University of California, Irvine, CA 92697, USA

⁶ Kavli Institute for Space and Astrophysics Research, Massachusetts Institute of Technology, 77 Massachusetts Ave., Cambridge, MA 02139-4307, USA

⁷ Department of Physics and Astronomy, Georgia State University, 25 Park Place, Suite 605, Atlanta, GA 30303, USA

⁸ Department of Physics and Astronomy, Wayne State University, 666 W. Hancock St., Detroit, MI 48201, USA

⁹ Department of Astronomy, University of Maryland, College Park, MD 20742, USA

¹⁰ Department of Astronomy and Astrophysics, Eberly College of Science, The Pennsylvania State University, 525 Davey Laboratory, University Park, PA 16802, USA

¹¹ Institute for Gravitation and the Cosmos, The Pennsylvania State University, University Park, PA 16802, USA

¹² Department of Physics and Astronomy, University of Leicester, University Road, Leicester, LE1 7RH, UK

¹³ Steward Observatory, University of Arizona, 933 North Cherry Avenue, Tucson, AZ 85721, USA

¹⁴ SRON Netherlands Institute for Space Research, Sorbonnelaan 2, 3584 CA Utrecht, The Netherlands

¹⁵ Leiden Observatory, Leiden University, PO Box 9513, 2300 RA Leiden, The Netherlands

¹⁶ Instituto de Astronomía, Universidad Nacional Autónoma de México, Ciudad de México, México

¹⁷ School of Physics and Astronomy, Raymond and Beverly Sackler Faculty of Exact Sciences, Tel Aviv University, Tel Aviv 69978, Israel

¹⁸ Department of Physics & Astronomy, University of Nevada, Las Vegas, 4505 South Maryland Parkway, Box 454002, Las Vegas, NV 89154-4002, USA

¹⁹ Instituto de Física, Pontificia Universidad Católica de Valparaíso, Casilla 4059, Valparaíso, Chile

²⁰ DARK, The Niels Bohr Institute, University of Copenhagen, Jagtvej 128, DK-2200 Copenhagen N, Denmark

²¹ University of Bath, Department of Physics, Claverton Down, BA2 7AY, Bath, UK

²² Cahill Center for Astrophysics, California Institute of Technology, Pasadena, CA 91125, USA

²³ Instituto de Física y Astronomía, Facultad de Ciencias, Universidad de Valparaíso, Gran Bretaña N 1111, Playa Ancha, Valparaíso, Chile

²⁴ Center for Exoplanets and Habitable Worlds, The Pennsylvania State University, University Park, PA 16802, USA

²⁵ Physics Department, California Polytechnic State University, San Luis Obispo, CA 93407, USA

²⁶ Department of Astronomy, University of California, Berkeley, CA 94720-3411, USA

²⁷ INAF IASF-Milano, Via Alfonso Corti 12, I-20133, Milan, Italy

²⁸ Crimean Astrophysical Observatory, P/O Nauchny, Crimea 298409¹⁰⁴

²⁹ Las Cumbres Observatory Global Telescope Network, 6740 Cortona Drive, Suite 102, Goleta, CA 93117, USA

³⁰ Fountainwood Observatory, Department of Physics FJS 149, Southwestern University, 1011 E. University Ave., Georgetown, TX 78626, USA

³¹ Department of Physics, The Pennsylvania State University, 104 Davey Laboratory, University Park, PA 16802, USA

³² Mullard Space Science Laboratory, University College London, Holmbury St. Mary, Dorking, Surrey RH5 6NT, UK

³³ Department of Physics and Astronomy, University of Wyoming, 1000 E. University Ave. Laramie, WY 82071, USA

³⁴ Department of Physics and Astronomy, University of Missouri, Columbia, MO 65211, USA

³⁵ Department of Astronomy and Astrophysics, University of California, Santa Cruz, 1156 High Street, Santa Cruz, CA 95064, USA

³⁶ Department of Physics and Astronomy, University of California, Riverside, CA 92521, USA

³⁷ Department of Physics and Astronomy, Western Kentucky University, 1906 College Heights Blvd. #11077, Bowling Green, KY 42101, USA

³⁸ Department of Astrophysical and Planetary Sciences, University of Colorado, Boulder, CO 80309, USA

³⁹ Dipartimento di Fisica e Astronomia “G. Galilei,” Università di Padova, Vicolo dell’Osservatorio 3, I-35122 Padova, Italy

- ⁴⁰ INAF-Osservatorio Astronomico di Padova, Vicolo dell'Osservatorio 5 I-35122, Padova, Italy
- ⁴¹ Department of Astronomy and Astrophysics, University of California Santa Cruz, 1156 High Street, Santa Cruz, CA 95064, USA
- ⁴² Institute for Computational Cosmology, Department of Physics, University of Durham, South Road, Durham DH1 3LE, UK
- ⁴³ Department of Physics and Astronomy, The University of Kentucky, Lexington, KY 40506, USA
- ⁴⁴ Instituto de Astrofísica de Canarias, Calle Vía Láctea s/n, E-38205 La Laguna, Tenerife, Spain
- ⁴⁵ Department of Earth, Environment and Physics, Worcester State University, Worcester, MA 01602, USA
- ⁴⁶ Centre for Extragalactic Astronomy, Department of Physics, University of Durham, South Road, Durham DH1 3LE, UK
- ⁴⁷ Pulkovo Observatory, 196140 St. Petersburg, Russia
- ⁴⁸ Miller Senior Fellow, Miller Institute for Basic Research in Science, University of California, Berkeley, CA 94720, USA
- ⁴⁹ Department of Astronomy, San Diego State University, San Diego, CA 92182, USA
- ⁵⁰ Oakwood School, 105 John Wilson Way, Morgan Hill, CA 95037, USA
- ⁵¹ School of Biological Sciences, University of Reading, Whiteknights, Reading, RG6 6AS, UK
- ⁵² Lick Observatory, P.O. Box 85, Mt. Hamilton, CA 95140, USA
- ⁵³ Astrophysics Science Division, NASA Goddard Space Flight Center, Mail Code 661, Greenbelt, MD 20771, USA
- ⁵⁴ Instituto de Astrofísica de Canarias, E-38200 La Laguna, Tenerife, Spain
- ⁵⁵ Departamento de Astrofísica, Universidad de La Laguna, E-38206 La Laguna, Tenerife, Spain
- ⁵⁶ Gran Telescopio Canarias (GRANTECAN), E-38205 San Cristóbal de La Laguna, Tenerife, Spain
- ⁵⁷ Spectral Sciences Inc., 4 Fourth Ave., Burlington, MA 01803, USA
- ⁵⁸ Eureka Scientific Inc., 2452 Delmer St. Suite 100, Oakland, CA 94602, USA
- ⁵⁹ Jet Propulsion Laboratory, California Institute of Technology, 4800 Oak Grove Drive, Pasadena, CA 91109, USA
- ⁶⁰ Department of Astrophysical Sciences, Princeton University, Princeton, NJ 08544, USA
- ⁶¹ Space Science Center, Morehead State University, 235 Martindale Dr., Morehead, KY 40351, USA
- ⁶² Department of Physics and Astronomy, York University, Toronto, ON M3J 1P3, Canada
- ⁶³ IPAC, Mail Code 100-22, California Institute of Technology, 1200 East California Boulevard, Pasadena, CA 91125, USA
- ⁶⁴ Department of Physics and Astronomy, University of California, Los Angeles, CA 90095, USA
- ⁶⁵ Carnegie Observatories, 813 Santa Barbara Street, Pasadena, CA 91101, USA
- ⁶⁶ Department of Physics and Astronomy, Texas A&M University, College Station, TX 77843-4242, USA
- ⁶⁷ George P. and Cynthia Woods Mitchell Institute for Fundamental Physics and Astronomy, Texas A&M University, College Station, TX 77843-4242, USA
- ⁶⁸ Astronomy Program, Department of Physics & Astronomy, Seoul National University, Seoul, Republic of Korea
- ⁶⁹ Santa Cruz Institute for Particle Physics and Department of Physics, University of California, Santa Cruz, CA 95064, USA
- ⁷⁰ Department of Physics and Astronomy, N283 ESC, Brigham Young University, Provo, UT 84602, USA
- ⁷¹ Physics Department, Technion, Haifa 32000, Israel
- ⁷² Minnesota Institute for Astrophysics, School of Physics and Astronomy, 116 Church Street S.E., University of Minnesota, Minneapolis, MN 55455, USA
- ⁷³ Korea Astronomy and Space Science Institute, Republic of Korea
- ⁷⁴ Department of Astronomy and Atmospheric Sciences, Kyungpook National University, Daegu 41566, Republic of Korea
- ⁷⁵ Department of Physics, University of Surrey, Guildford GU2 7XH, UK
- ⁷⁶ School of Physics, University of Melbourne, Parkville, VIC 3010, Australia
- ⁷⁷ Department of Physics, Western Michigan University, 1120 Everett Tower, Kalamazoo, MI 49008, USA
- ⁷⁸ Department of Astronomy, Columbia University, 550 W. 120th Street, New York, NY 10027, USA
- ⁷⁹ Departamento de Astronomía, Universidad de Chile, Camino del Observatorio 1515, Santiago, Chile
- ⁸⁰ Department of Astronomy, University of Massachusetts, Amherst, MA 01003, USA
- ⁸¹ University of Southampton, Highfield, Southampton, SO17 1BJ, UK
- ⁸² DiSAT, Università dell'Insubria, via Valleggio 11, I-22100, Como, Italy
- ⁸³ Instituto de Astronomía y Ciencias Planetarias, Universidad de Atacama, Copiapó, Chile
- ⁸⁴ Physics Department, United States Naval Academy, Annapolis, MD 21403, USA
- ⁸⁵ Department of Physics and Materials Science, The University of Memphis, 3720 Alumni Ave., Memphis, TN 38152, USA
- ⁸⁶ Harvard-Smithsonian Center for Astrophysics, 60 Garden Street, Cambridge, MA 02138, USA
- ⁸⁷ Department of Physics and Institute of Theoretical and Computational Physics, University of Crete, GR-71003 Heraklion, Greece
- ⁸⁸ IESL, Foundation for Research and Technology, GR-71110 Heraklion, Greece
- ⁸⁹ Department of Physics and Astronomy, Louisiana State University, Nicholson Hall, Tower Dr., Baton Rouge, LA 70803, USA
- ⁹⁰ Max Planck Institut für Astronomie, Königstuhl 17, D-69117 Heidelberg, Germany
- ⁹¹ Department of Physics, Faculty of Natural Sciences, University of Haifa, Haifa 31905, Israel
- ⁹² Department of Astronomy, University of Michigan, 1085 S. University Avenue, Ann Arbor, MI 48109, USA
- ⁹³ Department of Physics and Astronomy, Vanderbilt University, 6301 Stevenson Circle, Nashville, TN 37235, USA
- ⁹⁴ Laboratório Interinstitucional de e-Astronomia, Rua General José Cristino, 77 Vasco da Gama, Rio de Janeiro, RJ— Brazil
- ⁹⁵ Institute for Astronomy, 2680 Woodlawn Drive, Honolulu, HI 96822-1839, USA
- ⁹⁶ Department of Astronomy, University of Illinois Urbana-Champaign, 1002 W. Green Street, Urbana, IL 61801, USA
- ⁹⁷ Astronomical Institute "Anton Pannekoek," University of Amsterdam, Postbus 94249, NL-1090 GE Amsterdam, The Netherlands
- ⁹⁸ Kavli Institute for Space and Astrophysics Research, Massachusetts Institute of Technology, 77 Massachusetts Avenue, Cambridge, MA 02139-4307, USA
- ⁹⁹ Shanghai Jiao Tong University, 800 Dongchuan Road, Shanghai, 200240, People's Republic of China
- Received 2020 September 20; revised 2020 November 12; accepted 2020 November 25; published 2021 February 1*

Abstract

In this contribution, we achieve the primary goal of the active galactic nucleus (AGN) STORM campaign by recovering velocity–delay maps for the prominent broad emission lines ($\text{Ly}\alpha$, C IV, He II, and $\text{H}\beta$) in the spectrum

¹⁰⁰ Deceased, 2018 July 19.

¹⁰¹ Deceased, 2017 February 6.

¹⁰² Hubble Fellow.

¹⁰³ Packard Fellow.

¹⁰⁴ While the AAS journals adhere to and respect UN resolutions regarding the designations of territories (available at <http://www.un.org/press/en>), it is our policy to use the affiliations provided by our authors on published articles.

¹⁰⁵ Pappalardo Fellow.

of NGC 5548. These are the most detailed velocity–delay maps ever obtained for an AGN, providing unprecedented information on the geometry, ionization structure, and kinematics of the broad-line region. Virial envelopes enclosing the emission-line responses show that the reverberating gas is bound to the black hole. A stratified ionization structure is evident. The He II response inside 5–10 lt-day has a broad single-peaked velocity profile. The Ly α , C IV, and H β responses extend from inside 2 to outside 20 lt-day, with double peaks at ± 2500 km s $^{-1}$ in the 10–20 lt-day delay range. An incomplete ellipse in the velocity–delay plane is evident in H β . We interpret the maps in terms of a Keplerian disk with a well-defined outer rim at $R = 20$ lt-day. The far-side response is weaker than that from the near side. The line-center delay $\tau = (R/c)(1 - \sin i) \approx 5$ days gives the inclination $i \approx 45^\circ$. The inferred black hole mass is $M_{\text{BH}} \approx 7 \times 10^7 M_\odot$. In addition to reverberations, the fit residuals confirm that emission-line fluxes are depressed during the “BLR Holiday” identified in previous work. Moreover, a helical “Barber-Pole” pattern, with stripes moving from red to blue across the C IV and Ly α line profiles, suggests azimuthal structure rotating with a 2 yr period that may represent precession or orbital motion of inner-disk structures casting shadows on the emission-line region farther out.

Unified Astronomy Thesaurus concepts: Active galaxies (17); Astrophysical black holes (98); Supermassive black holes (1663); Active galactic nuclei (16); Reverberation mapping (2019)

1. Introduction

Active galactic nuclei (AGNs) are understood to be powered by accretion onto supermassive black holes in the nuclei of their host galaxies. On account of angular momentum, the accreting gas forms a disk on scales of a few to a few hundred gravitational radii, $R_g = GM_{\text{BH}}/c^2$, where M_{BH} is the mass of the central black hole. The accretion disk ionizes gas on scales of hundreds to thousands of R_g , which reprocesses the ionizing radiation into strong emission lines that are significantly Doppler-broadened by their motion in the deep gravitational potential of the black hole. However, the structure and kinematics of the “broad-line region” (BLR) remain among the long-standing unsolved problems in AGN astrophysics.

It is generally supposed that the BLR plays some role in the inflow and outflow processes that are known to occur on these spatial scales. There is evidence for disk structure in some cases (e.g., Wills & Browne 1986; Eracleous & Halpern 1994, 2003; Vestergaard et al. 2000; Strateva et al. 2003; Smith et al. 2004; Jarvis & McLure 2006; Gezari et al. 2007; Young et al. 2007; Lewis et al. 2010; Storchi-Bergmann et al. 2017), as well as evidence that gravity dominates the dynamics of the BLR (e.g., Peterson et al. 2004), although radiation pressure may also contribute (Marconi et al. 2008; Netzer & Marziani 2010). Perhaps the strongest evidence for a BLR with black-hole-dominated motions and a thick-disk geometry is the GRAVITY Collaboration’s spectroastrometry results showing the red and blue wings of the P α line spatially offset in opposite directions perpendicular to the jet in the nearest quasar, 3C 273 (Sturm et al. 2018).

The reverberation mapping (RM) technique (Blandford & McKee 1982; Peterson 1993, 2014) affords a means of highly constraining the BLR geometry and kinematics by measurement of the time-delayed response of the line flux to changes in the continuum flux as a function of Doppler velocity. The projection of the BLR velocity field and structure into the observables of Doppler velocity and time delay yields a “velocity–delay map.” Velocity–delay maps provide detailed information on the BLR geometry, velocity field, and ionization structure and can be constructed by analyzing the reverberating velocity profiles (Horne et al. 2004). This requires sustained monitoring of the reverberating spectrum with high signal-to-noise ratio (S/N) and high cadence to record the subtle changes in the line profiles.

1.1. The 2014 STORM Campaign on NGC 5548

To secure data suitable for velocity–delay mapping, NGC 5548 was the focus of an intensive monitoring campaign in 2014, the AGN Space Telescope and Optical Reverberation Mapping (AGN STORM) program. Ultraviolet (UV) spectra were obtained almost daily for 6 months with the Cosmic Origins Spectrograph on the Hubble Space Telescope (HST), securing 171 UV spectra covering rest-frame wavelengths 1130–1720 Å, including the prominent Ly α λ 1216 and C IV λ 1549 emission lines and the weaker Si IV λ 1397 and He II λ 1640 emission lines (De Rosa et al. 2015, hereafter Paper I). During the middle two-thirds of the campaign, observations with the Swift satellite provided longer-wavelength UV, 0.3–10 keV X-ray, and optical (*UBV*) continuum measurements (Edelson et al. 2015, hereafter Paper II). A major ground-based campaign secured imaging photometry (Fausnaugh et al. 2016, hereafter Paper III) with sub-diurnal cadence, including the *UBV* and Sloan *ugriz* bandpasses. Optical spectroscopic observations (Pei et al. 2017, hereafter Paper V) were also obtained, with 147 spectra covering the Balmer line H β λ 4861 and He II λ 4686.

Anomalous behavior in the emission-line response, known colloquially as the BLR Holiday, is discussed by Goad et al. (2016, hereafter Paper IV). Dehghanian et al. (2019, hereafter Paper X) present photoionization modeling using the absorption lines to diagnose how the ionizing spectral energy distribution changed during the BLR Holiday. Detailed fitting of a reverberating disk model to the HST, Swift, and optical light curves was accomplished by Starkey et al. (2016, hereafter Paper VI). The X-ray observations are discussed by Mathur et al. (2017, hereafter Paper VII). A comprehensive analysis modeling of the variable emission and absorption features is presented by Kriss et al. (2019, hereafter Paper VIII). The present manuscript, presenting velocity–delay maps derived from the spectral variations, is Paper IX.

Analysis of the STORM data sets has provided several breakthroughs and surprises that challenge our previous understanding of AGN accretion flows. One major breakthrough is the first clear measurement of interband continuum lags (Papers II and III), which can serve as a probe of the accretion disk temperature profile (Collier et al. 2001; Cackett et al. 2007). This tests a key prediction of the standard Shakura & Sunyaev (1973) disk theory, $T_{\text{eff}} \propto (M_{\text{BH}} \dot{M})^{1/4} r^{-3/4}$, where \dot{M} is the accretion rate. The STORM results are somewhat surprising, as follows:

1. From the continuum and broadband photometric light curves, cross-correlation analysis (Papers II and III), and detailed light-curve modeling (Paper VI), continuum lags and thus the disk size are larger than expected, by a factor of ~ 3 . Similarly, overlarge disks are inferred from microlensing effects in lensed quasar light curves (Poindexter et al. 2008; Morgan et al. 2010; Mosquera et al. 2013).
2. An excess lag in the U band, which samples the Balmer continuum, suggests that the long-lag problem may be an artifact of mixing short lags from the disk with longer lags from bound-free continuum emission reverberating in the larger BLR (Lawther et al. 2018; Chelouche et al. 2019; Korista & Goad 2019). More detailed modeling is needed to see whether this hypothesis can resolve the long-lag problem and rescue the standard disk theory. A more radical proposal invokes subluminal Alfvén-speed signals that trigger local viscosity enhancements at larger radii (Sun et al. 2020).
3. The time-delay spectrum is flatter than expected, $\tau \propto \lambda^1$ rather than $\tau \propto \lambda^{4/3}$. This implies a steeper temperature profile for the accretion disk, $T \propto r^{-1}$ rather than $r^{-3/4}$. The best-fit power-law slope is -0.99 ± 0.03 , some 7σ away from $-3/4$ (Paper VI). This might be evidence of nonzero stress at the innermost stable circular orbit, which can steepen the temperature profile to a slope of $-7/8$ (Mummery & Balbus 2020).
4. The accretion disk spectrum, inferred from the spectrum of the variable component of the light, is much fainter than predicted using the $T(r)$ profile inferred from $\tau(\lambda)$ (Paper VI). The disk surface seems to have a higher color temperature, $T(r)$ from the time-delay spectrum $\tau(\lambda)$, than its brightness temperature, $T(r)$ from the flux spectrum $F_\nu(\lambda)$. This low surface brightness and/or high color temperature is a further challenge to accretion disk theory. One possibility is large-grained gray dust obscuring the AGN, but that would produce a large mid-infrared excess that is not observed. Other possibilities are strong local temperature structures, or azimuthal structures in the disk thickness casting shadows on the irradiated disk surface.
5. The light curve needed to drive continuum reverberations in the UV and optical differs in detail from the X-ray light curve (Paper VI), being smoother and lacking the rapid variations seen in the X-rays. Gardner & Done (2017) have suggested that the observations imply that the standard inner disk is largely replaced by a geometrically thick Comptonized region. Another related possibility is tilting the inner disk to align with the black hole spin (Paper VI).

These continuum reverberation results pose serious challenges to the Shakura & Sunyaev (1973) accretion disk theory, sparking new thinking on the nature of black hole accretion disks. The emission-line variations also revealed some unexpected new phenomena, as follows:

1. There was a significant anomaly in the broad emission line behavior, the “BLR Holiday” (Paper IV). The emission lines track the continuum variations as expected in the first 1/3 of the STORM campaign, but then become fainter than expected in the latter 2/3, recovering just before the end. This anomalous period violates the expected behavior of

emission lines reverberating with time delays relative to the continuum. There are also significant changes in line intensity ratios, suggesting partial covering of a structured BLR, and/or changes in the shape of the ionizing spectrum. A plausible interpretation of this BLR Holiday is that part of the BLR is temporarily obscured to our line of sight and/or shielded from the ionizing radiation by a wind outflow, launched from the inner disk, that can transition between transparent and translucent states (Dehghanian et al. 2019b).

2. Significant broad and narrow absorption lines are seen in the UV spectra (Paper VIII). The narrow absorption lines exhibit equivalent width variations that correlate with the continuum variations. Here the time delays reflect recombination times, there being no light-travel time delays since absorption occurs only along the line of sight. The inferred density of $\sim 10^5 \text{ cm}^{-3}$ and location at $\sim 3 \text{ pc}$ are compatible with clouds in the narrow-line region (NLR; Peterson et al. 2013).

The focus of this paper is an echo-mapping analysis of the emission-line variations recorded in the STORM data. Section 2 briefly describes the HST and MDM Observatory spectra and the PREPSPEC analysis used to improve calibrations, and extract the mean and rms spectra and the continuum and emission-line light curves. Section 2.4 presents residuals to the PREPSPEC fit, including a “Barber-Pole” pattern suggestive of a rotating structure. In Section 3, we discuss the linearized echo model and MEMECHO fit to the emission-line light curves as time-delayed echoes of the 1150 Å continuum light curve, recovering the one-dimensional delay maps $\Psi(\tau)$ for each line. To model the anomalous BLR Holiday, we extended the MEMECHO model to include slowly varying line fluxes in addition to the reverberations modeled as echoes of the driving light curve. Section 4 presents our velocity–delay maps from MEMECHO analysis of the reverberating emission-line profiles, exhibiting the clear signature of an inclined Keplerian disk with a defined outer rim and front/back asymmetry. Comparisons with previous results are discussed in Section 5, and Section 6 closes with a summary of the main conclusions.

2. PREPSPEC Spectral Decomposition and Calibration Adjustments

Subtle features in the reverberating spectrum carry the information of interest; thus, echo-mapping analyses are sensitive to small calibration errors and inaccuracies in error bar estimates. The first stage of our analysis is therefore to fit a simple model decomposing the time-resolved spectra into a mean spectrum plus variable components each with their own rms spectrum and light curve. For the optical spectra, the narrow emission line components are then used to adjust the photometric calibration and wavelength scale and to equalize time-dependent spectral resolution. The PREPSPEC code developed and used for this purpose has been helpful in several previous studies (e.g., Grier et al. 2013) and is available online.¹⁰⁶

2.1. PREPSPEC Spectral Decomposition

The main results of our PREPSPEC analysis are given in Figure 1 for the ultraviolet HST spectra and in Figure 2 for the optical MDM spectra, where the left column gives the mean and

¹⁰⁶ <http://star-www.st-and.ac.uk/~kdh1/pub/ps/prepspec.tar.gz>

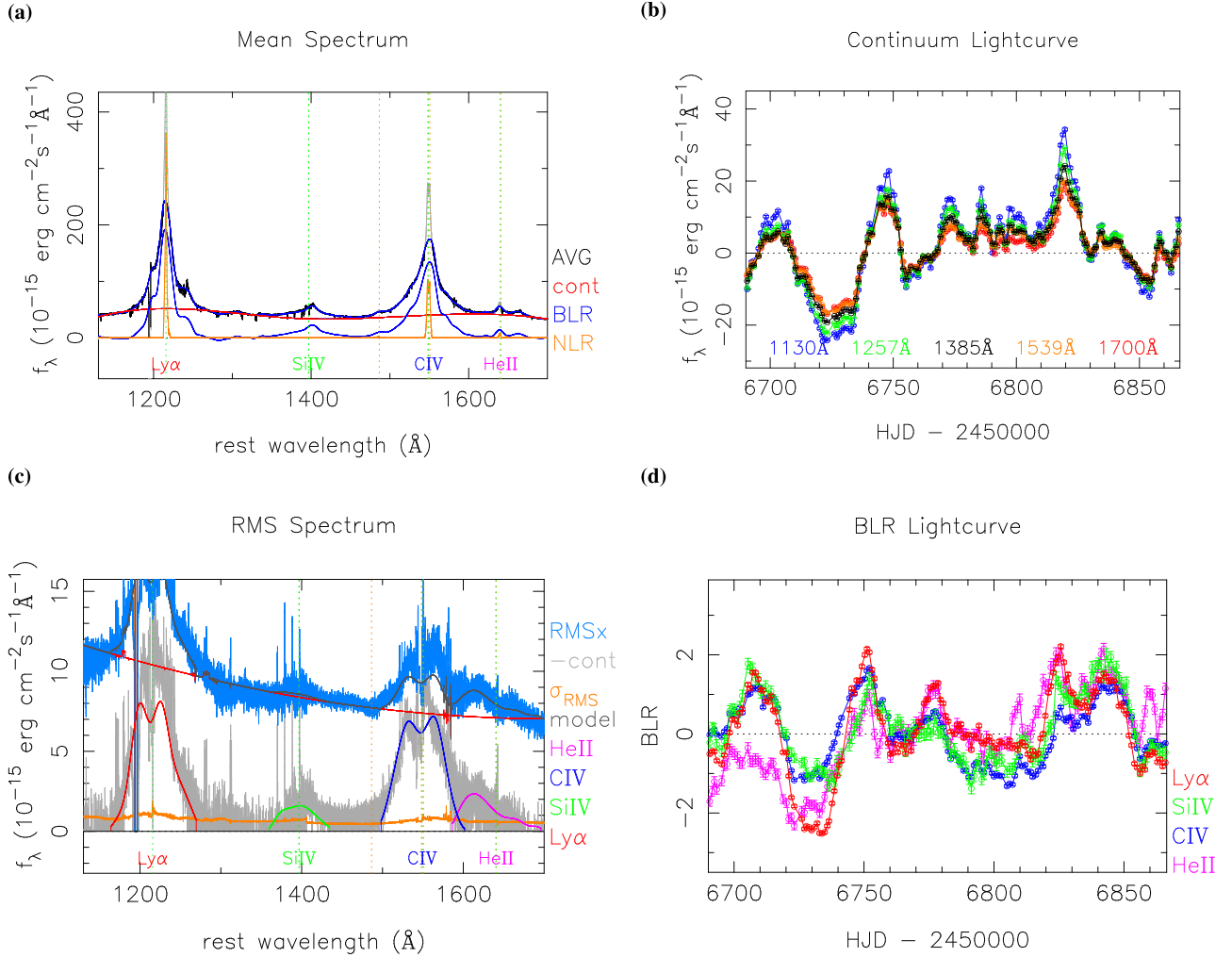


Figure 1. Results of the PREPSPEC fit to the HST data. (a) The mean spectrum $A(\lambda)$ (gray) is decomposed into the continuum $\bar{C}(\lambda)$ (red), the BLR spectrum $\bar{B}(\lambda)$ (blue), and the NLR spectrum $N(\lambda)$ (orange). (b) The continuum light curves, $C(\lambda, t)$, evaluated at five wavelengths across the spectrum. The amplitude is larger on the blue end than on the red end of the spectrum. (c) rms spectra before and after subtracting the continuum variations (blue and gray, respectively), and the corresponding uncertainties (yellow). Also shown are rms spectra for the fitted model (black), for the continuum variations $C(\lambda, t)$ (red), and for individual broad emission lines $B_i(\lambda)$ (color-coded as indicated). The blue slope of the continuum variations is evident. The strong Ly α and C IV lines have double-peaked profiles in their rms spectra. (d) BLR light curves $L_i(t)$, normalized to a median of 0 and a mean absolute deviation of 0.6745 (to match the MAD of an rms = 1 Gaussian).

rms spectra and the right column gives the continuum and emission-line light curves. PREPSPEC’s model for spectral variations is

$$F(\lambda, t) = A(\lambda) + B(\lambda, t) + C(\lambda, t), \quad (1)$$

where $A(\lambda)$ is the mean spectrum, $B(\lambda, t)$ models the broad emission line variations, and $C(\lambda, t)$ models continuum variations. We detail these components below.

PREPSPEC decomposes the *mean spectrum* as

$$A(\lambda) = N(\lambda) + \bar{B}(\lambda) + \bar{C}(\lambda), \quad (2)$$

where $N(\lambda)$ is the NLR spectrum, $\bar{B}(\lambda)$ is the BLR spectrum, and $\bar{C}(\lambda)$ is the continuum. These components are modeled as piecewise-cubic spline functions with different degrees of flexibility: stiff for the continuum, more flexible for the BLR, and very loose for the NLR. The emission-line components are forced to vanish outside a range of velocities around the rest wavelength of each line. After some experimentation, we set the emission-line windows to $\pm 1500 \text{ km s}^{-1}$ for the NLR lines, $\pm 10,000 \text{ km s}^{-1}$ for most of the BLR lines, and $\pm 6000 \text{ km s}^{-1}$

for H β . This decomposition can be used to measure emission-line strengths, widths, and velocity profiles in the mean spectrum. However, here we use it mainly to isolate the NLR component $N(\lambda)$, which PREPSPEC uses to improve the flux and wavelength calibrations.

PREPSPEC models the *continuum variations* as low-order polynomials in $\log(\lambda)$,

$$C(\lambda, t) = \sum_{k=1}^{N_c} C_k(t) X(\lambda)^k, \quad (3)$$

with N_c coefficients $C_k(t)$ that depend on time. Here

$$X(\lambda) = \frac{\log(\lambda^2/\lambda_1 \lambda_2)}{\log(\lambda_2/\lambda_1)} \quad (4)$$

interpolates linearly in $\log \lambda$ from -1 to $+1$ over the spectral range from λ_1 to λ_2 . We adopt cubic polynomials, $N_c = 4$, to represent the continuum variations in the HST spectra over the rest-frame wavelengths 1130–1720 Å and linear polynomials, $N_c = 2$, for the optical MDM spectral range 4500–5400 Å.

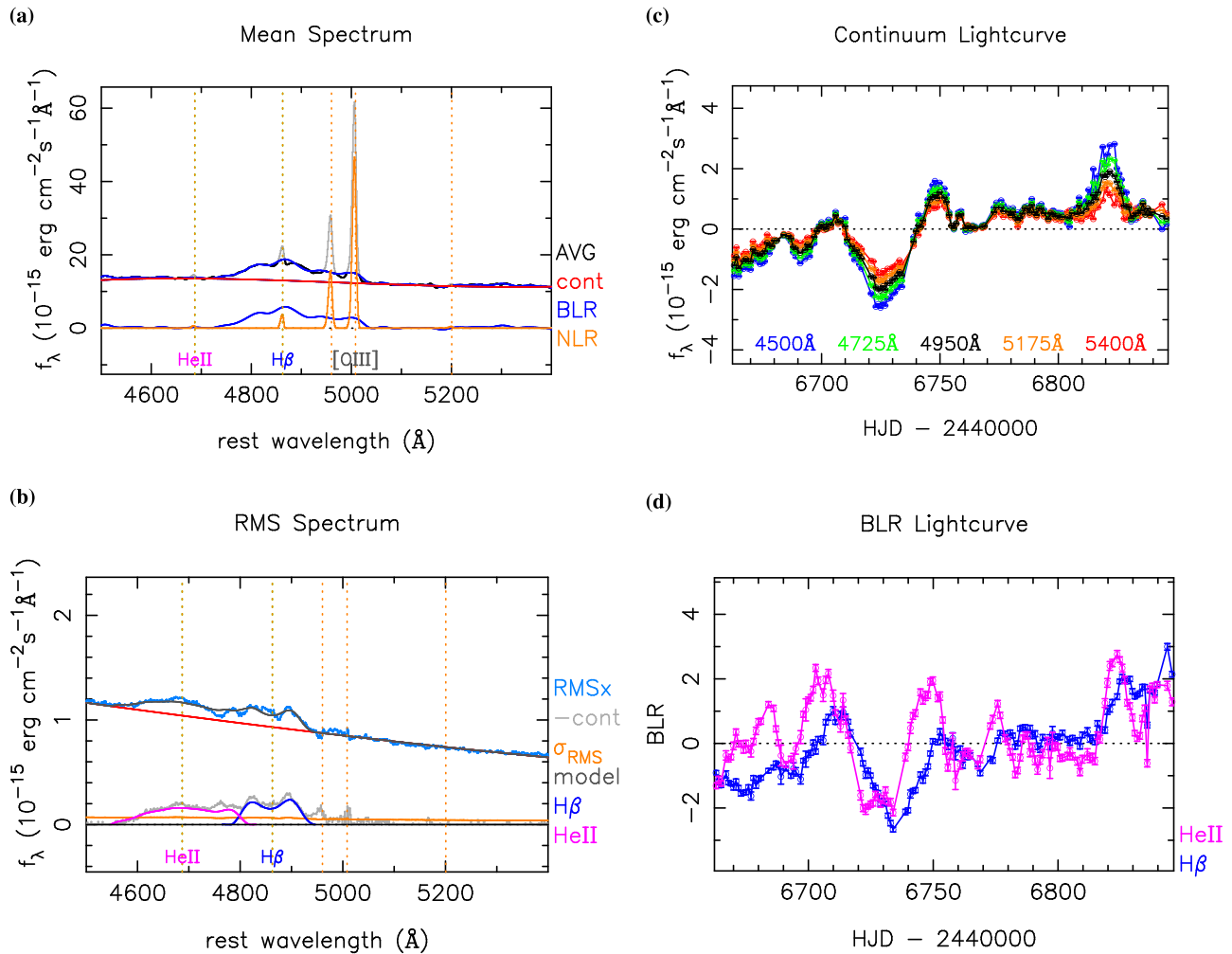


Figure 2. Same as in Figure 1, but here showing results of the PREPSPEC fit to the MDM data covering the optical spectral region including the broad H β and He II λ 4686 and narrow [O III] emission lines.

Lower values of N_c leave evident fit residuals, and higher values do not significantly improve the fit. PREPSPEC uses the full spectral range to define continuum variations relative to the mean spectrum, rather than fitting continua to individual spectra using defined relatively line-free continuum windows.

PREPSPEC models the *broad emission line variations* as

$$B(\lambda, t) = \sum_{\ell=1}^{N_\ell} B_\ell(\lambda) L_\ell(t), \quad (5)$$

thus representing the variable component of each line ℓ as a fixed line profile $B_\ell(\lambda)$ scaled by its light curve $L_\ell(t)$. The light curves are normalized to $\langle L_\ell \rangle = 0$ and $\langle L_\ell^2 \rangle = 1$. This constraint eliminates degeneracies between the model parameters and lets us interpret $B_\ell(\lambda)$ as the rms spectrum of the variations in line ℓ . In the same way as for the mean spectrum, the rms line profiles $B_\ell(\lambda)$ are modeled as piecewise-cubic spline functions and set to 0 outside the BLR window for that line. This separable model for the line variations assumes that each line has a fixed line profile that varies in strength with time. Residuals to the PREPSPEC fit then reveal the evidence for any changes in the line profile. Such changes contain the information we seek on the velocity–delay structure of the reverberating emission-line region and can reveal other

interesting phenomena such as the rotating pattern that we discuss in Section 2.4 below.

2.2. UV Spectra from HST

The UV spectra are the same HST spectra discussed and analyzed with cross-correlation methods in Paper I. These spectra exhibit several narrow absorption systems that interfere with our analysis. We used the spectral modeling analysis in Paper VIII to identify wavelength regions affected by narrow absorption features and remove the narrow absorption effects. The fluxes and uncertainties in these regions are divided by the model transmission function, restoring to a good approximation the flux that would have been observed in the absence of the absorption while also expanding the error bars to appropriately reflect the lower number of detected photons.

Similarly, a Lorentzian optical depth profile provided an approximate fit to the broad wings of the geocoronal Ly α absorption. We divided the observed fluxes and their error bars by the model transmission, approximately compensating for the geocoronal Ly α absorption at moderate optical depths. The opaque core of the geocoronal line was beyond repair, and we omit those wavelengths (1214.3–1216.8 Å) from our analysis.

The main results of our PREPSPEC fit to the HST spectra are shown in Figure 1, where the left and right columns show the

spectral and temporal components of the model, respectively.

In Figure 1(a), the mean spectrum $A(\lambda)$ is decomposed into the NLR spectrum $N(\lambda)$ (orange), the BLR spectrum $\bar{B}(\lambda)$ (blue), and the continuum $\bar{C}(\lambda)$ (red). The BLR spectrum has very strong, broad Ly α and C IV emission extending to $\pm 10,000$ km s $^{-1}$, with weaker counterparts in Si IV and He II. As PREPSPEC failed to robustly separate Ly α and N V, we opted to model the Ly α +N V blend as a single line. The NLR spectrum is dominated by Ly α and C IV with narrow emission peaks also at N V and He II. A few narrow absorption features remain uncorrected that will not adversely affect our analysis. Figure 1(b) shows the continuum light curves, $C(\lambda, t)$, evaluated at five wavelengths across the spectrum. Continuum variations with a median absolute deviation (MAD) of 16% relative to the continuum in the mean spectrum are detected with S/N ≈ 500 . The amplitude is larger at 1130 Å on the blue end than at 1700 Å on the red end of the spectrum. Figure 1(c) shows the rms spectra and Figure 1(d) the corresponding BLR light curves. The blue slope of the continuum variations is again evident in the rms spectrum. The BLR variations are detected with high S/N, ~ 400 for Ly α , ~ 300 for C IV, ~ 120 for He II, and ~ 80 for Si IV. The BLR light curves generally resemble those of the continuum, but with time delays and other systematic differences that are distinct for each line. The strong Ly α and C IV lines are single peaked in the mean spectrum but double peaked in the rms spectrum, suggesting that the variations arise from a disk-like BLR. Variations are detected in N V $\lambda 1240$ on the red wing of Ly α , in Si IV $\lambda 1393$, and in He II $\lambda 1640$.

2.3. Optical Spectra from MDM

Optical spectra from the MDM Observatory were presented and analyzed with a cross-correlation analysis in Paper V. Ground-based spectra taken at facilities other than MDM were excluded from this analysis in order to have a consistent and homogeneous data set taken with the same instrument, same spectral resolution, and so on. The ground-based MDM spectra were taken through a 5"-wide slit and extracted with a 15" aperture, under variable observing conditions. As a result, each spectrum has a slightly different calibration of flux, wavelength, and spectral resolution. While these residual calibration errors are most evident in the regions around narrow emission lines, they contribute to a smaller extent throughout the spectrum.

To compensate for this, the PREPSPEC model $M(\lambda, t)$ includes small adjustments to the calibrations:

$$M(\lambda, t) = p(t) \left(F - \Delta\lambda(t) \frac{\partial F}{\partial \lambda} + \Delta s(t) \frac{\partial^2 F}{\partial \lambda^2} \right). \quad (6)$$

Here the calibration-adjusted model is $F(\lambda, t)$, given by Equation (1), and the small time-dependent adjustments to the calibration are parameterized by $p(t)$ to model imperfect photometry, $\Delta\lambda(t)$ for small changes to the wavelength scale, and $\Delta s(t)$ for small changes in the spectral resolution. PREPSPEC models $\ln p(t)$ to ensure that $p(t)$ remains positive. The median of $p(t)$ is set to unity, since typically a minority of the observed spectra are low owing to slit losses and imperfect pointing or variable atmospheric transparency. While PREPSPEC can model $\ln p(t)$, $\Delta\lambda(t)$, and $\Delta s(t)$ as low-order polynomials of $\log \lambda$, the wavelength dependence of these calibration adjustments was not

needed over the relatively short wavelength span of the MDM data analyzed here.

The main results of our PREPSPEC analysis of the MDM spectra are shown in Figure 2. This optical spectral region includes the broad H β and He II $\lambda 4686$ emission lines and narrow [O III] emission lines. In the mean spectrum, Figure 2(a), H β and [O III] are strong but He II is very weak. H β also has a narrow component. In the rms spectrum, Figure 2(b), the continuum is bluer than in the mean spectrum, the He II line is much stronger, and the [O III] line is very weak (if well calibrated, this emission line should not vary at all and thus should not show a signal in the rms spectrum). Note that the profile of broad H β is single peaked in the mean but double peaked in the rms spectrum. The continuum and emission-line light curves are shown in Figures 2(c) and (d), respectively. Maxima and minima in the He II light curve occur a few days earlier than their counterparts in the H β light curve.

2.4. Patterns in Residuals to the PREPSPEC Fit

Figure 3 presents results of an analysis of the residuals of the PREPSPEC fit to the UV HST (left) and optical MDM (right) spectra. The PREPSPEC model assumes for each line a fixed line profile that changes in normalization only. The residuals to the PREPSPEC fit thus present a visualization of the evidence for variations in the velocity profiles of the emission lines. They also serve as a check on the success of the absorption-line corrections, the calibration adjustments based on the narrow [O III] emission lines, and the accuracy of the error estimates.

The top panels, Figures 3(a) and (b), present the fitted PREPSPEC model as a grayscale “trailed spectrogram,” with wavelength increasing to the right and time upward. Here horizontal bands arise from the continuum variations, and vertical bands mark the locations of emission lines. The middle panels, Figures 3(c) and (d), show residuals after subtracting the PREPSPEC model from the observed spectra. There are acceptably small fine-scale residuals near the strong narrow [O III] lines at 4959 and 5007 Å, indicating the good quality of the calibrations. In Figure 3(d) the evident patterns moving toward the center of the H β line arise from reverberations affecting the line wings first and then moving toward the line center. We find below that these can be interpreted as reverberation of H β -emitting gas with a Keplerian velocity field. There are also stationary features near 4750, 4880, and 4970 Å that decrease over the 180-day span of the observations, indicating a gradual decrease in the emission-line flux with time.

In Figure 3(c) the dominant residuals near the C IV line exhibit an intriguing helical “Barber-Pole” pattern with stripes moving from red to blue across the line profile. This Barber-Pole pattern may be present also in the Ly α residuals, but less clearly so owing to higher levels of systematic problems created by the absorption-line corrections and blending with N V. We see no clear evidence of the Barber-Pole pattern in the H β residuals, where the reverberation signatures are stronger. The peak-to-trough amplitude of these features in C IV is $\pm 8\%$ of the continuum flux density—far too large to be ascribed to calibration errors in the HST spectra.

The bottom panels, Figures 3(e) and (f), show the mean $\mu(\lambda)$ and rms $\chi(\lambda)$ of the *normalized* residuals, scaled by the error bars. The $\chi(\lambda)$ curves (blue) rise near the emission lines, where significant line profile variations are being detected, and level off in the continuum to values below unity, 0.81 for the HST and 0.89 for the MDM spectra. These low values indicate that

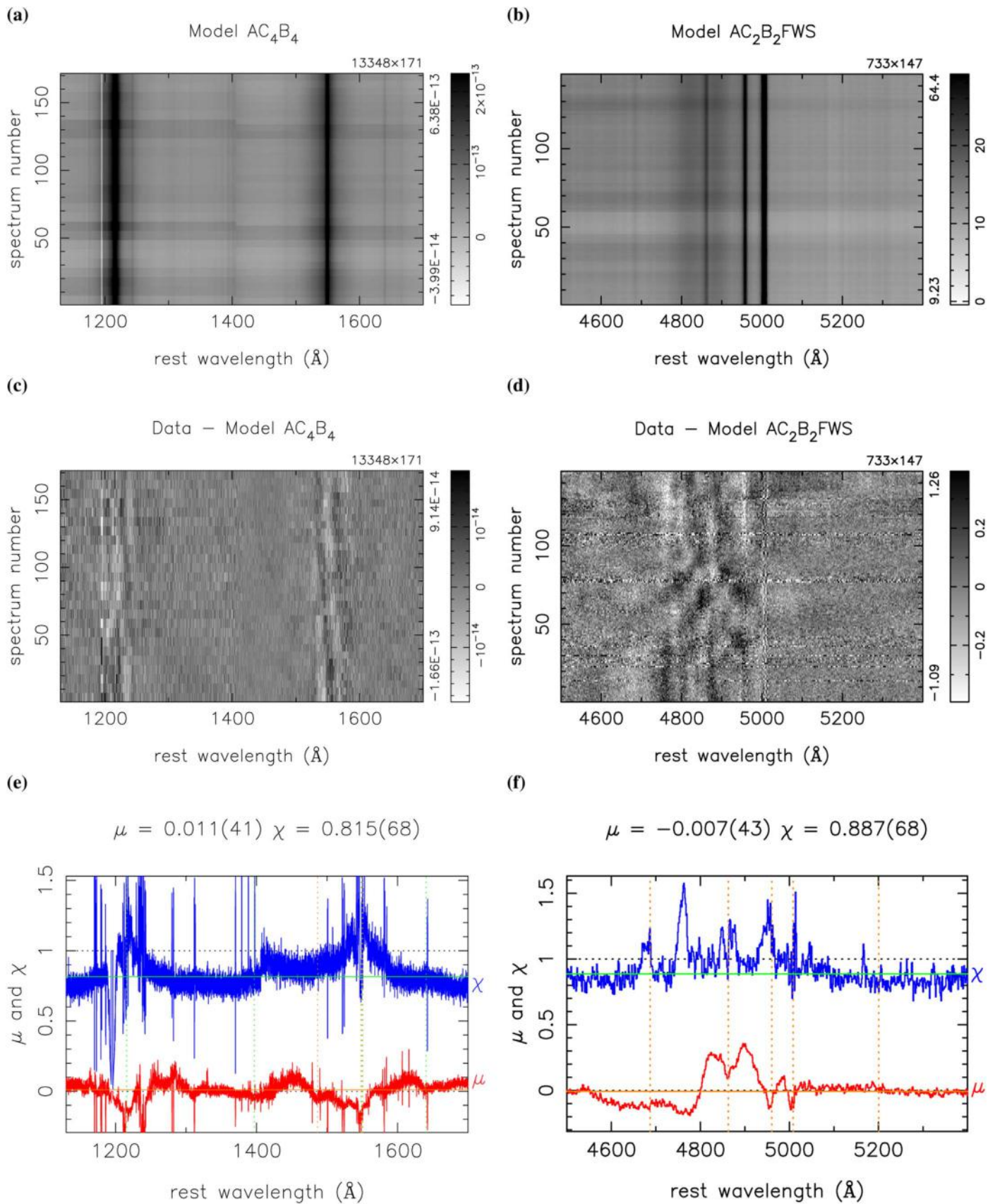


Figure 3. Model (a, b) and residuals (c, d) of the PREPSPEC fit to the HST (left) and MDM (right) data. The bottom panels show the mean (red) and rms (blue) over time of the normalized residuals for (e) HST and (f) MDM. Note in panel (c) the helical “Barber-Pole” pattern of stripes moving from red to blue across the C IV and Ly α line profiles. The model specification key includes components A = average spectrum, C_n = continuum polynomial with n parameters, B_n = BLR for n emission lines, and for the MDM data the calibration adjustments F = flux, W = wavelength, and S = seeing.

rms residuals are smaller than expected from the nominal error bars. For the MEMECHO analysis to follow, we multiply the nominal error bar spectra by these factors.

2.5. Interpretation of the Barber-Pole Pattern

The Barber-Pole pattern is a new phenomenon in AGNs. Manser et al. (2019) report a similar pattern of stripes moving from red to blue across the infrared Ca II triplet line profiles arising from a thin ring or disk of gas orbiting a white dwarf. The 2 hr period is stable over several years, prompting its interpretation as due to an orbiting planetesimal perturbing the debris disk around the white dwarf.

We tentatively interpret the Barber-Pole pattern in NGC 5548 as evidence for azimuthal structure, perhaps caused by the shadows cast by the vertical structure associated with precessing spiral waves or orbiting material or streamlines near the base of a disk wind, which rotate around the black hole with a period of ~ 2 yr. This 2 yr period is estimated based on the impression from Figure 3(c) that the stripes move halfway across the C IV profile during the 180-day campaign, so that 180 days is $1/4$ of the period of the rotating pattern. This is clearly just a rough estimate. From the velocity–delay maps discussed in Section 4 below, we infer a black hole mass $M_{\text{BH}} \approx 7 \times 10^7 M_{\odot}$ and a disk-like BLR geometry extending from 2 to 20 lt-day with an inclination $i \approx 45^\circ$. A 2 yr orbital period then occurs at $R/c \approx 4$ days, or $R \approx 1000 G M_{\text{BH}}/c^2$, compatible with the inner region of the BLR. The corresponding Kepler velocity is $V = \sqrt{G M_{\text{BH}}/R} \approx 9000 \text{ km s}^{-1}$, and this projects to $V \sin i \approx 7000 \text{ km s}^{-1}$ for $i \approx 45^\circ$. These rough estimates are compatible with the observed velocity amplitude of the Barber-Pole stripes in the C IV residuals.

The effect must be stronger on the far side of the disk, to produce Barber-Pole features that move from red to blue across the line profile, and weaker on the near side, where they would be seen moving from blue to red. This front-to-back asymmetry might be due to a bowl-shaped BLR geometry, so that the near side of the BLR disk is strongly foreshortened. However, the velocity–delay maps discussed in Section 4 indicate that the response is stronger on the near side than on the far side of the disk. Alternatively, if the inner disk is tilted toward us, perhaps due to a misaligned black hole spin, then material orbiting there could rise above the outer-disk plane, to cast shadows on the far side of the outer disk, and then dip below the plane to avoid casting shadows on the near side of the outer disk.

Detailed modeling beyond the scope of this paper may test the viability of these and other interpretations. Further monitoring of NGC 5548 with HST may be helpful to determine whether the Barber-Pole phenomenon is stable or transient, whether its period is stable or changing, and whether the stripes always go from red to blue or sometimes from blue to red across the C IV profile.

3. MEMECHO Analysis: Velocity–Delay Mapping

Our echo-mapping analysis is performed with the MEMECHO code, which is described in some detail by Horne (1994). Its ability to recover velocity–delay maps from simulated HST data is demonstrated (Horne et al. 2004), and it has recently been subjected to blind tests (Mangham et al. 2019). We outline below the assumptions and methodology and then present and discuss the results of our MEMECHO analysis of the HST and MDM data on NGC 5548.

Echo mapping assumes that a compact source of ionizing radiation is located at or near the center of the accretion flow. Photons emitted here shine out into the surrounding region, causing local heating and ionization of gas, which then emits a spectrum characterized by emission lines as it cools and recombines. Reprocessing times are expected to be short and dynamical times long compared to light-travel times. As distant observers, we see the response from each reprocessing site with a time delay τ from the light-travel time and a Doppler shift ν from the line-of-sight velocity. Thus, the reverberating emission-line spectrum encodes information about the geometry, kinematics, and ionization structure of the accretion flow—to be more specific, that part of the flow that emits the reverberating emission lines.

To decode this information, we interpret the observed spectral variations as time-delayed responses to a driving light curve. By fitting a model to the reverberating spectrum $F(\lambda, t)$, we reconstruct a two-dimensional wavelength–delay map $\Psi(\lambda, \tau)$. This effectively slices up the accretion flow on isodelay surfaces, which are paraboloids coaxial with the line of sight with a focus at the compact source. Each delay slice gives the spectrum of the response, revealing the fluxes and Doppler profiles of emission lines from gas located on the corresponding isodelay paraboloid. The resulting velocity–delay maps $\Psi(\nu, \tau)$ provide two-dimensional images of the accretion flow, one for each emission line, resolved on isodelay and isovelocity surfaces.

3.1. Linearized Echo Model

The full spectrum of ionizing radiation is not observable, and so an observed continuum light curve, $C(t)$, is adopted as a proxy. At each time delay τ , the responding emission-line light curve $L(t)$ is then some nonlinear function of the continuum light curve $C(t - \tau)$ shifted to the earlier time $t - \tau$. In addition, the observed line and continuum fluxes include constant or slowly varying background contributions from other light sources, such as narrow-line emission and starlight from the host galaxy. To model these backgrounds and account for the nonlinear BLR responses, MEMECHO employs a *linearized* echo model, with reference levels C_0 for the continuum and L_0 for the line flux, and a tangent-curve approximation to variations around these reference levels. Thus, the continuum light curve $C(t)$ is decomposed as

$$C(t) = C_0 + \Delta C(t), \quad (7)$$

and the emission-line light curve,

$$L(t) = L_0 + \int \Psi(\tau) \Delta C(t - \tau) d\tau, \quad (8)$$

is a convolution of the continuum variations with a delay map $\Psi(\tau)$, giving the one-dimensional delay distribution of the emission-line response. We find that this linearized echo model fails to provide a good fit to the NGC 5548 data. We therefore generalize the model to allow a time-dependent echo background level, $L_0(t)$. This extension is straightforward.

3.2. Maximum Entropy Regularization

Maximum entropy regularization keeps the model light curves $C(t)$ and $L_0(t)$ and the delay maps $\Psi(\tau)$ positive and “as smooth as possible” while fitting the data. Referring to these

functions generically as $p(t)$, the entropy is

$$S(p) = \sum_t w(t) [p(t) - q(t) - p(t) \ln(p(t)/q(t))], \quad (9)$$

measured with weights $w(t)$ and relative to a default function $q(t)$. We obtain $q(t)$ by Gaussian smoothing of $p(t)$, with an FWHM of 1, 2, and 4 days for the driving light curve, the delay map, and the echo background, respectively. These choices control the flexibility of the functions. The weights $w(t)$ provide additional control on relative flexibility among the three functions.

For fits to reverberating spectra, the MEMECHO model simply adds a wavelength dimension to the echo light curve, $L(t) \rightarrow L(\lambda, t)$, to the response distribution, $\Psi(\tau) \rightarrow \Psi(\lambda, \tau)$, and to the background variations, $L_0(t) \rightarrow L_0(\lambda, t)$. These two-dimensional functions are then regularized with the entropy defined relative to default functions that average in both directions.

The MEMECHO fit is accomplished by iteratively adjusting the functions p to minimize

$$Q(p, D) = \chi^2(p, D) - \alpha S(p). \quad (10)$$

Here $\chi^2(p, D)$ quantifies the “badness of fit” to the N data D , assuming Gaussian noise with known error bars. The Lagrange multiplier α controls the trade-off between fitting the data (small χ^2) and being simple (large S). In practice, α is initially large, and a series of converged fits is constructed with decreasing χ^2 and increasing S , stopping when the fit is judged to be satisfactory ($\chi^2/N \approx 1$) and the model not overly complex.

3.3. Delay Maps $\Psi(\tau)$ for NGC 5548

Figure 4 shows the results of our MEMECHO fit to five continuum and six emission-line light curves of NGC 5548. The light-curve data are from the PREPSPEC analysis of the HST and MDM spectra, described in Section 2. MEMECHO fits all light curves simultaneously, recovering a model for the driving light curve $C(t)$, and for each echo light curve a delay map $\Psi(\tau)$ and a background light curve $L_0(t)$. The driving light curve $C(t)$ (bottom panel of Figure 4) is the 1150 Å continuum light curve, with the reference level C_0 (red line) set at the median of the 1150 Å continuum data. Above this are 10 echo light curves (right) and corresponding delay maps (left), where the light-curve data (black points with green error bars) can be directly compared with the fitted model (blue curves). We model four continuum light curves, at 1300, 1450, and 1700 Å from the HST spectra and at 5100 Å from the MDM spectra, as echoes of the 1150 Å continuum. The reverberating emission lines are He II $\lambda 1640$ and He II $\lambda 4686$, then H β and Ly α , and finally Si IV and C IV. The MEMECHO fit accounts for much of the light-curve structure as echoes of the driving light curve but requires significant additional variations $L_0(t)$ (red curves), particularly during the BLR Holiday indicated by gray shading in Figure 4.

The fit shown in Figure 4 requires $\chi^2/N = 1$ separately for the driving light curve and for each of the echo light curves, where there are $N = 171$ and 147 data points for the HST and MDM light curves, respectively. The model light curves (delay maps) are evaluated on a uniform grid of times (delays) spaced by $\Delta t = 0.5$ days, linearly interpolated to the times of the observations. The delay maps span a delay range of 0–50 days.

The delay maps $\Psi(\tau)$ are of primary interest because they indicate the radial distributions from the central black hole over which the continuum and emission lines are responding to variations in the driving radiation. The continuum light curves exhibit highly correlated variations that are well fit by exponential delay distributions strongly peaked at $\tau = 0$. The median delay, increasing with wavelength, is ~ 1 day at 1700 Å and ~ 5 days at 5100 Å. The echo background has only small variations, indicating that the linearized echo model is a very good approximation for the continuum light curves.

The emission-line light curves require more extended delay distributions and larger variations in their background levels. The background variations are similar, but not identical, for the six emission-line light curves. The two He II light curves require tight delay distributions peaking at $\tau = 0$, with half the response inside ~ 5 days and 3/4 inside 10 days, and some low-level structure at 20–40 days. The background light curves have a “slow wave” with a 100-day timescale, somewhat different for the two lines, and smaller-amplitude 10-day structure. The slow-wave background for He II $\lambda 1640$ is rising from HJD 6690 to 6750 (really HJD–2,450,000), while that for He II $\lambda 4686$ is more constant. Both backgrounds then decline to minima around HJD 6800 and then rise until 6840. The constant background for He II $\lambda 1640$ prior to HJD 6690 and for He II $\lambda 4686$ after HJD 6850 is not significant since there are no data during these intervals.

The H β response exhibits the most extended delay distribution, with a peak at 7 days, half the response inside 14 days, 3/4 inside 23 days, minor bumps at 25 and 40 days, and falling to 0 at 50 days. The need for this extended delay map is evident in the H β light curve, for example, to explain the slow H β decline following peaks at HJD 6705 and 6745. The Ly α response is more confined than H β with a peak at 3 days, half the response inside 7 days, 3/4 inside 15 days, and bumps at 26 and 35 days. Si IV and C IV are similar, with peaks at 5 and 7 days, respectively.

The slow-wave backgrounds $L_0(t)$ for all these lines fall slowly from HJD 6740 to 6820 and then rise more rapidly to a peak at HJD 6840. This corresponds approximately to the anomalous BLR Holiday period discussed in Paper IV, indicated by gray shading in Figure 4, during which the emission lines became weak relative to the continuum. Note also a smaller dip from HJD 6715 to 6740 that serves to deepen the emission-line decline between the two peaks, particularly for C IV. A small peak near HJD 6810 accounts for emission-line peaks in C IV, Si IV, and He II $\lambda 1640$ that have no clear counterpart in the continuum light curves.

Note that the model and background light curves (blue and red curves in Figure 4) exhibit numerous small spikes in addition to smoother 100-day and 10-day structure. These spikes correspond to data points that are too high or too low, relative to their error bars, to be fit by the smooth default light curve that maximizes the entropy. The largest offender is a low point in the H β and He II $\lambda 4686$ light curves near HJD 6837, which likely represents a calibration error. These outliers could seriously damage the delay maps. The spikes are less prominent if we relax the fit to a higher χ^2/N , but then the fit to the relatively low S/N Si IV light curve is less satisfactory. Fortunately, because our model has time-dependent backgrounds that can develop sharp spikes where required, the delay maps remain relatively smooth and insensitive to these outliers.